

MINI-REVIEW

Real-time detection of breast cancer at the cellular level

Gary E. Carver¹  | Sarah A. Locknar¹ | Donald L. Weaver² | Janet L. Stein³  | Gary S. Stein² 

¹Omega Optical, Brattleboro, Vermont

²Department of Pathology and Laboratory Medicine, University of Vermont Cancer Center, Burlington, Vermont

³Department of Biochemistry, University of Vermont Cancer Center, Burlington, Vermont

Correspondence

Gary E. Carver, Omega Optical, 21 Omega Drive, Brattleboro 05301, VT.
Email: gcarver@omegafilters.com.

Funding information

The National Institutes of Health, Grant/Award Numbers: P01 CA082834, U01 CA196383; The Charlotte Perelman Fund for Cancer Research

Abstract

Novel optoelectronic instrumentation has been developed for the multispectral imaging of autofluorescence emitted by metabolic fluorophores. The images resolve individual cells while spectra are collected for each pixel in the images. These datacubes are generated at a rate of 10 per second—fast enough for surgical guidance. The data is processed in real time to provide a single color-coded image to the surgeon. To date, the system has been applied to fresh, ex vivo, human surgical specimens and has distinguished breast cancer from benign tissue. The approach is applicable to in vivo measurements of surgical margins and needle-based optical biopsies. Ongoing work demonstrates that the system has great potential for translation to a hand-held probe with high sensitivity and specificity.

KEYWORDS

autofluorescence, breast cancer, multispectral imaging, surgical margin

1 | INTRODUCTION

More women are diagnosed with breast cancer than any other cancer (Jemal, Center, DeSantis, & Ward, 2010). This year, an estimated 252,710 women in the United States will be diagnosed with invasive breast cancer. Treatment of the cancer typically involves a lumpectomy or mastectomy. A continuing problem in tumor resection is the detection of residual cancer cells in areas adjacent to excision. Over 20% of breast cancer surgeries require follow-up excision within 3 months. To a great extent, this problem is caused by insufficient surgical margin guidance. As a result, patients are faced with protracted periods of concern, morbidity, and additional cost.

1.1 | Potential optical applications in oncology

The current surgical paradigm involves removal of tissue, delivery to pathology, and gross margin assessment while the patient is still in surgery, or frequently, histological evaluation after they go home. The pathology workup consists of formalin fixation followed by paraffin embedding, slicing to a few microns thick and hematoxylin and eosin (H&E) staining followed by a microscopic assessment. This well-established process takes a significant amount of time.

Additional surgery is often required following pathological examination, particularly when disease is at or in close proximity to surgical margins. Augmenting the traditional H&E evaluation with a real-time microscopic assessment of the surgical margin by the surgeon or pathologist via a hand-held instrument would reduce follow-up surgeries and associated costs and contraindications. To take this idea even further, a diagnostic optical biopsy method would reduce the prevalence of invasive surgical biopsies (roughly 27% of all biopsies) that are performed before lumpectomies in the United States each year.

1.2 | Metabolics

The transformation from normal tissue to cancer involves a number of changes to the morphology, gene expression, and metabolic processes within the tissues. The high metabolic rate of cancer cells moves them to a more hypoxic situation where glycolysis becomes more prevalent than typical aerobic cellular respiration through the electron-transport chain. This in turn leads to an increase in the reduced form of nicotinamide adenine dinucleotide (NADH)/flavin adenine dinucleotide (FAD) ratio (or the redox ratio). Simultaneously, hemoglobin oxygenation near the tumor decreases as the growing

tumor extracts more oxygen from the blood. To facilitate angiogenesis, the extracellular collagen matrix changes its composition and morphology (Luparello, 2013; Wu et al., 2018).

Britton Chance and others established the fluorescence properties of the NADH and FAD back in the late 1950s (Chance & Jöbsis, 1959). His work has seen a resurgence as instrumentation has improved to detect the weak emission from unlabelled specimens. Recently, both Yu and Heikal (2009) and Ostrander et al. (2010) have observed an increase in cytosolic (NADH) due to increased glycolysis in cancer cells—the Warburg effect (Georgakoudi & Quinn, 2012). Yu and Heikal (2009) reported that the average NADH concentration in breast cancer cells = $168 \pm 49 \mu\text{M}$, while the average NADH concentration in normal breast cells = $99 \pm 37 \mu\text{M}$. The ratio of NADH/FAD is a self-normalizing metric as the intensity of the two fluorophores is similarly affected by optical scatter. There are several other common intrinsic chromophores—vitamin A/retinol, lipofuscin/lipoproteins, collagen, melanin, and so forth (Croce & Bottioli, 2014), but they appear not to be major indicators of breast pathology.

1.3 | Overview of optical methods

Optical methods for characterizing the health of breast tissue encompass techniques that observe purely morphological features such as optical coherence tomography (OCT), reflectance, and second-harmonic generation (SHG), and techniques that sense molecular effects including diffuse optical imaging (DOI), fluorescence, fluorescence lifetime (FLIM), and Raman scattering. It is not unusual for researchers to combine modalities to reach higher levels of sensitivity and specificity.

OCT can provide micron-resolution structural information within a few millimeter of the surface of the sample at video rates (Wang, Xu, & Boppart, 2017). It is often performed as a point-scanning method with a laser source and can easily be combined with other techniques that provide molecular information. SHG requires a high-power pulsed laser source, typically at near-infrared (NIR) wavelengths, so is often used in conjunction with multiphoton fluorescence techniques including two- or three-photon excitation and FLIM modalities. The second-harmonic signal is generated by noncentrosymmetric molecules in the specimen such as collagen.

Reflectance imaging is the most common as virtually any method that shines a light off the surface to create an image (in the surgeon's eye or a camera) is using reflectance. To provide more contrast, multi- or hyperspectral information about the surface can be acquired by changing the illumination wavelength or splitting the detected wavelength into channels (Volynskaya et al., 2008; Zhu, Palmer, Breslin, Harter, & Ramanujam, 2008). A widefield hyperspectral camera system (400–1,700 nm) by Headwall Photonics is being used in brain cancer applications, (Fabelo et al.,) and a home-built system with 40- μm resolution has been demonstrated to distinguish mammary tumor from surrounding tissue using multispectral reflectance in rats (Panasyuk et al., 2007). Reflectance on the microscopic scale can be combined with confocal optics to gain some morphological depth information. Hyperspectral reflectance

with polarization imaging is commercially available for the microscopic detection of skin cancer (Vasevi et al.,).

DOI employs NIR spectroscopic mapping (roughly 650–1,100 nm) of the breast to identify hemoglobin oxygen saturation levels, lipid, and water concentrations in partially compressed breast tissues to create a several mm-resolution two-dimensional map of tumor distribution (Anderson et al., 2015). While informative, the hemoglobin saturation level alone is insufficient to identify tumors because it depends on total hemoglobin concentration (or perfusion) of the tumor (Grosenick, Rinneberg, Cubeddu, & Taroni, 2016). Researchers get around this limitation by simultaneously measuring water content (which increases) and lipid content (which decreases) in a tumor. This “optical mammogram” is finding utility in the noninvasive monitoring of neoadjuvant treatment as its nonionizing radiation is preferred over X-rays and is significantly less expensive than magnetic resonance imaging.

The excitation maxima of many intrinsic chromophores (tryptophan, NADH, FAD, collagen, elastin, and vitamin A) are in the UVa region of the spectrum (400–320 nm; Breslin et al., 2004; Chance & Jöbsis, 1959; Shi et al., 2017). Early on, Chance measured changes in NADH concentration with muscle contraction (Chance & Jöbsis, 1959). More recently, reflectance coupled with fluorescence using 405 nm excitation has been used to identify precancerous lesions on fallopian tubes (McAlpine et al., 2011). Mauna Kea has found commercial success in detecting intrinsic fluorescence in gastrointestinal (GI), lung, and urological applications using a microendoscope with 488 nm excitation (Thiberville et al., 2007; Zellweger et al., 2001). They theorize that the bulk of the contrast in lung is generated by the elastin component of the basement membrane (Thiberville et al., 2007). Our group has also used autofluorescence at 488 nm excitation to visualize human breast cancer xenographs in mouse (Carver, Locknar, Morrison, Ramanujan, & Farkas, 2014).

Another widely adopted method for excitation of intrinsic chromophores is the use of two- or three-photon pulsed NIR laser (multiphoton) to excite molecules that typically absorb in the ultraviolet (UV). This has been used to calculate intracellular NADH concentrations in normal and cancer cell lines (Yu & Heikal, 2009) and in simultaneous imaging of NADH, FAD, and collagen (Georgakoudi & Quinn, 2012; Wu et al., 2018; You et al., 2018). These methods give a detailed microscopic image with a field-of-view of $\sim 0.5 \text{ mm}^2$ or more and a rate of roughly 2 s/image with $\sim 14 \text{ mW}$ of laser power incident on the sample (You et al., 2018). The pulsed nature of the NIR laser also allows for FLIM measurements. When coupled with optical filters, the emission decay curves of NADH, FAD, and other molecules can be calculated and mapped with microscopic resolution (Walsh et al., 2013). Although historically a slow technique, recent developments at MIT have increased the rate to roughly 1.5 s/frame (0.6 mm^2 ; Giacomelli, Sheikine, Verdeh, Connolly, & Fujimoto, 2015). While this technique is very powerful in its ability to simultaneously image metabolic and structural elements at a subcellular level, it has the potential to cause cellular damage from localized heating and three-photon absorption processes of DNA bases. Another disadvantage is cost—the femtosecond

lasers used in this technique are cost-prohibitive for large-scale deployment in small hospitals and clinics.

Vibrational imaging and characterization of the molecular structure of the tissue is performed by infrared (IR; absorption or Fourier-transform infrared [FTIR]) or Raman (inelastic scattering) spectroscopy. The sharp vibrational peaks can be spectrally unmixed into their component spectra, so these methods contain a wealth of chemical information. FTIR and IR absorption imaging have been effective at identifying cancer on fixed sections (Kumar, Desmedt, Larsimont, Sotiriou, & Goormaghtigh, 2013; Surmacki, Musial, Kordek, & Abramczyk, 2013) but they are slow (~5 min/image) and as transmissive techniques, not translatable to an in vivo application. Raman scattering in general is a very weak signal that requires significant integration time and laser power (up to 10 mW at the sample; Surmacki et al., 2013). There are methods (surface-enhanced Raman and resonance Raman scattering, coherent anti-Stokes Raman scattering, etc.) to increase the signal, but these require complicated sample preparation techniques (in the case of surface-enhanced methods) and laser systems (CARS) that render them impractical for in vivo applications (Ellis, Cowcher, Ashton, O'Hagan, & Goodacre, 2013).

1.4 | Commercial availability

There are several OCT-based systems that are already approved or are seeking FDA approval, for applications ranging from ophthalmology (Optovue, Fremont, CA, Topcon Medical, Oakland, NJ) to cardiovascular (Conavi Medical, North York, ON, Canada) to real-time characterization of GI lesions (NinePoint Medical, Bedford, MA) and skin (Michelson Diagnostics, Maidstone, Kent, UK). These are purely for structural characterization of the tissues and none are applied to breast cancer. Mauna Kea Technologies' microendoscope for autofluorescence imaging has recently been approved for neurosurgical applications. This system uses either 488 or 800 nm excitation with detection of total fluorescence. It does not provide spectral information about the emitting chromophores and is not approved for use in breast cancer. FotoFinder (Bad Birnbach, Germany) has developed a line of white light and fluorescence

dermoscopes for clinical use and in this same space, Newton Technologies (Lyon, France) has developed a hyperspectral reflectance imaging system. Neither of these are approved for use in breast cancer applications.

2 | APPROACH

Our approach is based on multispectral imaging of fluorescence related to NADH and FAD. As described below, the scanning rates generate 10 datacubes per second. Coupled with real-time image processing, our system is faster than most of the techniques presented in the previous section. Surgeons tell us that frame rates should be less than about 1 per second. Further, our design minimizes photon flux on the tissue such that live cells can be scanned with no sign of photo-induced damage.

2.1 | Optical design

The left side of Figure 1 shows a schematic of our optical design. The two scanning mirrors generate an *xy* spatial scan of the tissue, while the optical fiber arrays are used to collect spectra for each pixel in the images. The spectra are acquired during the dwell time of the excitation spot on the sample. Timing and synchronization is important in our design. Excitation is provided by a pulsed laser beam, which propagates through the spatial scanners towards the tissue sample. As the two mirrors are scanned in an *x-y* raster pattern, the focused spot on the sample is always conjugate with the entrance face of the multimode fiber that is connected to the fiber array. Since fluorescence from biological materials typically occurs within 1–5 ns after excitation, both reflected and photoexcited signals propagate back to the fiber entrance face before the mirrors can move appreciably. This allows the mirrors to de-scan back-propagating photons such that light from the focused spot stays conjugate with the fiber. As a result, scanning confocal systems can generate maps (or "images") with spatial resolution at or near the

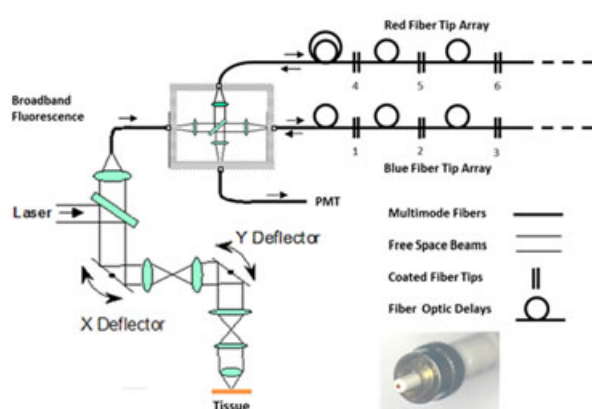


FIGURE 1 Optical schematic (left) and system in pathology (right) [Color figure can be viewed at wileyonlinelibrary.com]

laser spot size. In the current system, the laser is focused at $NA = 0.24$ to a $1.2\text{-}\mu\text{m}$ diameter spot and scanned over an adjustable field (that can be zoomed from 50 to $500\text{ }\mu\text{m}$). Our fiber optic spectrometer is based on a serial array of reflecting spectral elements, delay lines between these elements, and a single element detector. After excitation by a laser pulse, broadband fluorescence from the sample propagates into the array via the confocal aperture. Light of the first wavelength band reflects from the first element, and light of the N th wavelength band reflects from the N th element. Each wavelength is mapped into a specific time slot. Each delay line is equal to the length of the laser pulse. Our spectral elements are composed of coated fiber tips—five coated fiber tips on the blue leg of a beam splitter and another five coated tips on the red leg of a beam splitter (see inset in Figure 1). Each coated tip reflects light up to a transition wavelength. Each spectral bin is bounded by two of the transition wavelengths. Light from the blue array is detected in time before light from the red array. The key advantage of this design is speed. The 10 spectral bins are acquired during the dwell time of each pixel in the spatial scan ($2.5\text{ }\mu\text{s}$ in the current design). A full datacube including images at all 10 bins is generated in 0.1 s.

Beyond speed, this design has several additional advantages. First, the laser is pulsed with a duty cycle of $1/25$. The low duty cycle avoids heating and photodamage in live tissue. Second, wavelength bin centers and band-pass widths can be arranged with varying widths and spacings matched to a given application. The spectral widths and spacings in designs based on single bulk gratings are constrained by the diffraction equation. Third, the wavelength separation method has no influence on spatial scanning fidelity. A map of a given color will spatially register with a map of another color. Fourth, each polarization state is reflected in a similar manner. Fifth, the new design naturally integrates with confocal optics. This cost-effective design functions without either a diffraction grating or a camera.

As mentioned above, our design employs a short excitation pulse and therefore exposes the tissue to less radiation than approaches using detector arrays that must stare at the tissue for extended periods. By design, our system employs laser pulses with a low duty cycle ($1/25$), and has a dwell time fraction on any given pixel of $2.5\text{E} - 6\text{ s/pixel}$ divided by 0.1 s/frame equaling $2.5\text{E} - 5$. The incident laser is typically set to 5 mW —considered a safe level in the surgical suite (Vogel & Venugopalan, 2003). Total average joules per second directed at a given resolved spot on the tissue is therefore $5 \times (1/25) \times 2.5\text{E} - 5 \times 10 = 5\text{E} - 5\text{ mW}$. This amount of power is briefly focused into a $1\text{-}\mu\text{m}$ spot and is well tolerated by the tissue. This power density in a small spot leads to far less heating than occurs when the same power density is applied to a mm or cm diameter area (Carver, 1992). Further, the blue/violet/soft UV light used in this study is not energetic enough to excite or damage DNA. Models including a reasonable scatter coefficient, absorption coefficient, and quantum yield predict signals in the nW range—as is observed. Single photon excitation with the associated shallow penetration depths is appropriate for assessing exposed margins in a surgical cavity.

The picture on right side of Figure 1 shows the system deployed in the pathology suite at UVM Medical. The translated system will feature a hand-held probe compatible with surgical applications. The optics can also be miniaturized for insertion into the bore of a biopsy needle for presurgical optical biopsy applications.

2.2 | Image processing

As discussed above, our system generates 10 black and white images every 0.1 s—one for each spectral bin. Clearly, a method is needed to combine these images into a useful format for use by the surgeon. One such method utilizes Spectral Angle Mapping (SAM) as described in Figure 2. The dot product between two vectors \mathbf{a} and \mathbf{b} is equal to the magnitude of \mathbf{a} times the magnitude of \mathbf{b} times the cosine of the angle between \mathbf{a} and \mathbf{b} . As indicated in the drawing, this calculation determines what component of \mathbf{a} points in the direction of \mathbf{b} . The dot product is also the sum of $a_i \cdot b_i$ over all values of i , where i denotes a given dimension of \mathbf{a} and \mathbf{b} . In our case, we assign \mathbf{a} to S (the signal vector), and \mathbf{b} to R (the reference vector). Both S and R are 10-dimensional vectors where N corresponds to our 10 spectral bins. In practice, R is the set to the spectral distribution where cancer exists, and S the spectral distribution in an unknown tissue sample. The value of cosine theta is computed in real time for each pixel in our images. The brightness of a pixel in the live image presented to the surgeon is set to the brightest spectral bin (to maximize contrast), while the color of a pixel in the image is set according to the value of cosine theta. Higher values of cosine theta are indicative of disease and are colored yellow to red, while lower values of cosine theta are indicative of normal tissue and are colored blue to green. This method is self-normalizing, because the effects of optical scatter alter the numerator and denominator by the same factor. Other real-time spectral processing algorithms can also be used, including redox ratio. We expect spectral angle mapping with 10-spectral bins to equal or surpass the sensitivity and specificity of redox ratio mapping. In summary, our novel instrumentation detects relevant intrinsic fluorophores and presents actionable data to the surgeon in real time.

2.3 | Fresh ex vivo samples

We have scanned fresh ex vivo human breast tissue samples from 35 patients under IRB 16-710 at the University of Vermont Medical

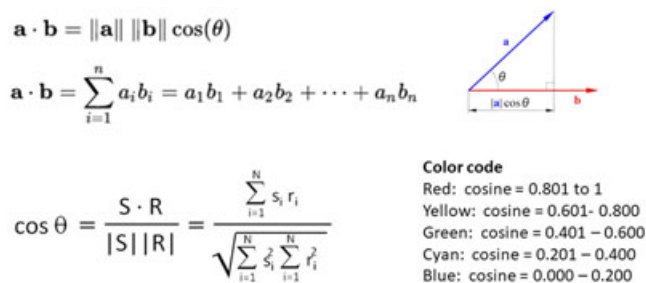


FIGURE 2 Spectral angle mapping mathematics [Color figure can be viewed at wileyonlinelibrary.com]

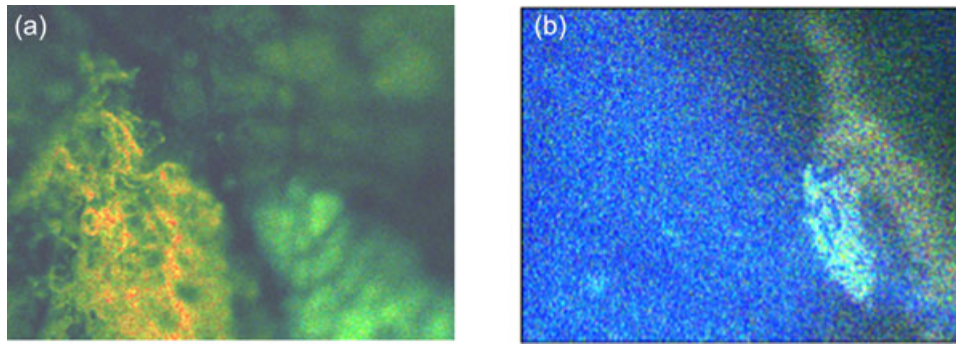


FIGURE 3 SAM images (500 μm field) for cancer (a) and benign tissue (b) [Color figure can be viewed at wileyonlinelibrary.com]

Center (UVM Medical, Burlington, VT). With patient consent, our protocol allows us to receive/scan/return small portions of tissue in the pathology suite within minutes of excision in the surgical suite. A portion of a known tumor is sliced from the main specimen and placed in a dish under our objective lens. Scanning cells within about 20 min is important for ensuring that we are evaluating live cells with representative concentrations of metabolic fluorophores. All marking, fixation, and staining is done after our optical scans are complete. The 35 patients included both lumpectomies and mastectomies. Tissue samples were scanned using one of three laser wavelengths (375, 405, or 488 nm). The system was originally designed with 10 spectral bins spanning the visible spectrum, but during the course of this study, we determined that the signal above about 625 nm was weak in most specimens. In the results section, bins above this level have been omitted.

3 | RESULTS

Signal to noise is low with excitation at 488 nm, stronger at 405 nm, and quite robust at 375 nm. Only 375 nm excitation is expected to induce fluorescence from both NADH and FAD (Croce & Bottioli, 2014; Georgakoudi & Quinn, 2012; Shi et al., 2017). During these experiments, we have created reference vectors on the tumors and then observed images across the tumor margins. Several images show adipose cells in green and nearby fibrous tissue in red. The margins appear maximally evident with 375 nm excitation. Figure 3a shows a fibrous area with significant red colorization adjacent to adipose with green colorization. Routine H&E staining was applied to the invasive breast cancer specimen that contained tissue corresponding to this image. The fluorescent image was overlaid on the H&E image to demonstrate correlation between the multispectral signals and the tumor where the pseudo color (yellow to red) represents the tumor epithelium. The spectral vector used in Figure 3a is presented in Figure 4. The signals are rather high at wavelengths where NADH-related fluorescence is expected, and low at wavelengths where FAD-related fluorescence is expected. Figure 3b shows a spectral angle mapping (SAM) image obtained from a benign fibroadenoma using the same spectral vector. The image is correctly colored blue indicating the absence of cancer. Fibroadenomas are benign proliferations of epithelium and stroma from the breast lobule. Figure 4 presents the

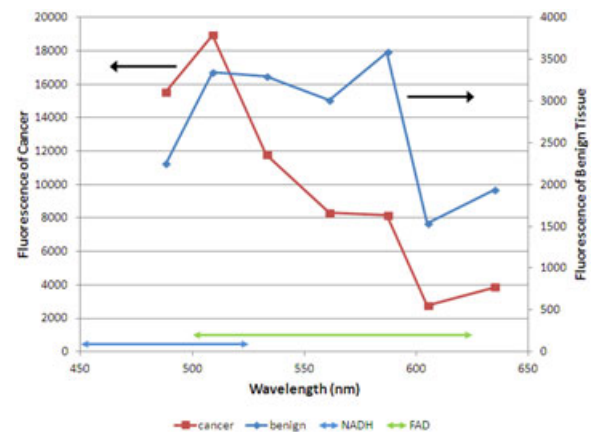


FIGURE 4 Spectra associated with images in Figure 3 [Color figure can be viewed at wileyonlinelibrary.com]

average spectrum from this blue-coded image. The signals are much lower than the previous sample, with lower relative intensity at NADH-related wavelengths and higher relative intensity at FAD-related wavelengths. These data sets establish that our system can easily distinguish tumors from benign lesions.

A key element in our plan going forward is to harvest cells from the yellow/red areas (tumor cells) and equivalent blue/green areas from breast reduction surgeries (normal cells) via laser capture microdissection (LCM), such that the cells can be profiled by RNA sequencing and the transcriptomic profiles compared. This will allow us to correlate compromised cells with metabolic features observed by our scanner but not necessarily by structural pathology.

4 | DISCUSSION

Our images, obtained by multispectral confocal imaging, display structural information that has been correlated with structural pathology. Our spectra, and the corresponding color coding in the images, are related to metabolic features. This combination of structural and metabolic information has been harvested in real time with no signs of cellular damage.

Once fully translated, our optics will be redesigned into an ergonomic hand-held probe tethered to a cart supporting a color-coded display for use by surgeons in the operating room. This new capability will shift clinical practice by enabling surgeons to assess tumor margins in real time to inform the extent of surgical resection. Color-coded images will cover a 5 mm field of view in 0.1 s. Translation of this capability to a hand-held probe is crucial for implementation by surgeons (You et al., 2018). Validation studies will be extended beyond correlations with H&E staining. We will also harvest cancer and normal cells identified by our optical system via LCM for subsequent analysis by genetic (DNA-encoded regulatory information) and epigenetic (non-DNA-encoded regulatory information) approaches. These efforts are expected to show that our optical contrast is related to cellular metabolism rather than blood and oxygenation issues. It is anticipated that the multispectral imaging approach we have developed for breast cancer will support optical imaging of other solid tumors.

Our results were obtained with spectral vectors that were obtained with a software tool that averages the spectra of all pixels in the given image. As a result, a cancer vector can be "polluted" with noncancerous pixels. Even under that circumstance, the clear differences between the two images in Figure 3 are still observed. Ongoing work will "purify" the vectors by averaging over restricted regions-of-interest rather than the full images. The vectors can also be improved by harvesting more wavelengths in the NADH band, and using fewer, wider bins in the FAD band. These enhancements should allow for the straightforward separation of normal tissue and fibroadenoma from malignant tissue such as invasive ductal and invasive lobular cancer. It will be informative to correlate our images with the ER/PR/Her2 status of each patient.

5 | CONCLUSIONS

A multispectral confocal scanning system has been developed for the real-time detection of fluorescence related to the cellular concentration of NADH and FAD. Images and spectra collected by the system show definable differences between cancer and fibroadenoma. Once translated into a hand-held probe, surgeons will have the capability to monitor surgical margins at the cellular level during lumpectomies. This capability will reduce the necessity for follow-up surgical procedures. Multispectral imaging has the potential to support needle biopsy procedures, and stain-free histopathology.

ACKNOWLEDGMENTS

Support for the studies was provided by Omega Optical, grants from The National Institutes of Health (P01 CA082834 and U01 CA196383) and the Charlotte Perelman Fund for Cancer Research.

ORCID

Gary E. Carver  <http://orcid.org/0000-0001-8124-3191>

Janet L. Stein  <http://orcid.org/0000-0002-2474-6822>

REFERENCES

- Anderson, P. G., Kainerstorfer, J. M., Sassaroli, A., Krishnamurthy, N., Homer, M. J., Graham, R. A., & Fantini, S. (2015). Broadband optical mammography: Chromophore concentration and hemoglobin saturation contrast in breast cancer. *PLoS One*, *10*, e0117322.
- Breslin, T. M., Xu, F., Palmer, G. M., Zhu, C., Gilchrist, K. W., & Ramanujam, N. (2004). Autofluorescence and diffuse reflectance properties of malignant and benign breast tissues. *Annals of Surgical Oncology*, *11*(1), 65–70.
- Carver, G. E. (1992). Scanned photoluminescence with high spatial resolution in semi-insulating GaAs and InP: Aspects of surface passivation and photodegradation. *Semiconductor Science and Technology*, *7*, A53–A58.
- Carver, G. E., Locknar, S. A., Morrison, W. A., Krishnan ramanujan, V., & Farkas, D. L. (2014). High-speed multispectral confocal biomedical imaging. *Journal of Biomedical Optics*, *19*, 36016.
- Chance, B., & Jöbsis, F. (1959). Changes in fluorescence in a frog sartorius muscle following a twitch. *Nature*, *184*, 195–196.
- Croce, A. C., & Bottiroli, G. (2014). Autofluorescence spectroscopy and imaging: A tool for biomedical research and diagnosis. *European Journal of Histochemistry*, *58*(4), 2461.
- Ellis, D. I., Cowcher, D. P., Ashton, L., O'Hagan, S., & Goodacre, R. (2013). Illuminating disease and enlightening biomedicine: Raman spectroscopy as a diagnostic tool. *Analyst*, *138*, 3871–3884.
- Fabelo, H., Ortega, S., Kabwama, S., Callico, G. M., Bulters, D., Szolna, A., ... Sarmiento, R. (2016). HELICOiD project: A new use of hyperspectral imaging for brain cancer detection in real-time during neurosurgical operations. *SPIE Commercial + Scientific Sensing and Imaging*. Baltimore, MD, USA.
- Georgakoudi, I., & Quinn, K. P. (2012). Optical imaging using endogenous contrast to assess metabolic state. *Annual Review of Biomedical Engineering*, *14*, 351–367.
- Giacomelli, M. G., Sheikine, Y., Vardeh, H., Connolly, J. L., & Fujimoto, J. G. (2015). Rapid imaging of surgical breast excisions using direct temporal sampling two photon fluorescent lifetime imaging. *Biomedical Optics Express*, *6*(11), 4317–4325.
- Grosenick, D., Rinneberg, H., Cubeddu, R., & Taroni, P. (2016). Review of optical breast imaging and spectroscopy. *Journal of Biomedical Optics*, *21*(9), 091311.
- Jemal, A., Center, M. M., DeSantis, C., & Ward, E. M. (2010). Global patterns of cancer incidence and mortality rates and trends. *Cancer Epidemiology, Biomarkers and Prevention*, *19*, 1893–1907.
- Kumar, S., Desmedt, C., Larsimont, D., Sotiriou, C., & Goormaghtigh, E. (2013). Change in the microenvironment of breast cancer studied by FTIR imaging. *Analyst*, *138*, 4058.
- Luparello, C. (2013). Aspects of collagen changes in breast cancer. *Journal of Carcinogene Mutagene*, *S13*(007)
- McAlpine, J. N., El Hallani, S., Lam, S. F., Kalloger, S. E., Luk, M., Huntsman, D. G., ... Lane, P. M. (2011). Autofluorescence imaging can identify preinvasive or clinically occult lesions in fallopian tube epithelium: A promising step towards screening and early detection. *Gynecologic Oncology*, *120*, 385–392.
- Ostrander, J. H., McMahon, C. M., Lem, S., Millon, S. R., Brown, J. Q., Seewaldt, V. L., & Ramanujam, N. (2010). Optical redox ratio differentiates breast cancer cell lines based on estrogen receptor status. *Cancer Research*, *70*(11), 4759–4766.
- Panasuk, S. V., Yang, S., Faller, D. V., Ngo, D., Lew, R. A., Freeman, J. E., & Rogers, A. E. (2007). Medical hyperspectral imaging to facilitate residual tumor identification during surgery. *Cancer Biology & Therapy*, *6*(3), 439–446.
- Shi, L. Y., Lu, L. Y., Harvey, G., Harvey, T., Rodriguez-Contreras, A., & Alfano, R. R. (2017). Label-free fluorescence spectroscopy for detecting key biomolecules in brain tissue from a mouse model of Alzheimer's disease. *Scientific Reports*, *7*.

- Surmacki, J., Musial, J., Kordek, R., & Abramczyk, H. (2013). Raman imaging at biological interfaces: Applications in breast cancer diagnosis. *Molecular Cancer*, 12, 48.
- Thiberville, L., Moreno-Swirc, S., Vercauteren, T., Peltier, E., Cavé, C., & Bourg Heckly, G. (2007). In vivo imaging of the bronchial wall microstructure using fibered confocal fluorescence microscopy. *American Journal of Respiratory and Critical Care Medicine*, 175(1), 22–31.
- Vasevi, F., MacKinnon, N., Saager, R., Kelly, K. M., Maly, T., Chave, R., ... Farkas, D. L. (2016). Multimode optical dermoscopy (SkinSpect) analysis for skin with melanocytic nevus. *Proceedings of the SPIE*. Bellingham, WA. <https://doi.org/10.1117/12.2214288>
- Vogel, A., & Venugopalan, V. (2003). Mechanisms of pulsed laser ablation of biological tissues. *Chemical Reviews*, 103(2), 577–644.
- Volynskaya, Z., Haka, A. S., Bechtel, K. L., Fitzmaurice, M., Shenk, R., Wang, N., ... Feld, M. S. (2008). Diagnosing breast cancer using diffuse reflectance spectroscopy and intrinsic fluorescence spectroscopy. *Journal of Biomedical Optics*, 13, 024012.
- Walsh, A. J., Cook, R. S., Manning, H. C., Hicks, D. J., Lafontant, A., Arteaga, C. L., & Skala, M. C. (2013). Optical metabolic imaging identifies glycolytic levels, subtypes and early-treatment response in breast cancer. *Cancer Research*, 73(20), 6164–6174.
- Wang, J., Xu, Y., & Boppart, S. A. (2017). Review of optical coherence tomography in oncology. *Journal of Biomedical Optics*, 22(12), 121711.
- Wu, S., Huang, Y., Tang, Q., Li, Z., Horng, H., Li, J., ... Li, H. (2018). Quantitative evaluation of redox ratio and collagen characteristics during breast cancer chemotherapy using two-photon intrinsic imaging. *Biomedical Optics Express*, 9(3), 1375–1388.
- You, S., Tu, H., Chaney, E. J., Sun, Y., Zhao, Y., Bower, A. J., ... Boppart, S. A. (2018). Intravital imaging by simultaneous label-free autofluorescence-multiharmonic microscopy. *Nature Communications*, 9, 2125.
- Yu, Q., & Heikal, A. A. (2009). Two-photon autofluorescence dynamics imaging reveals sensitivity of intracellular NADH concentration and conformation to cell physiology at the single-cell level. *Journal of Photochemistry and Photobiology. B, Biology*, 95(1), 46–57.
- Zellweger, M., Goujon, D., Conde, R., Forrer, M., van den Bergh, H., & Wagnières, G. (2001). Absolute autofluorescence spectra of human healthy, metaplastic, and early cancerous bronchial tissue in vivo. *Applied Optics*, 40(22), 3784–3791.
- Zhu, C., Palmer, G. M., Breslin, T. M., Harter, J., & Ramanujam, N. (2008). Diagnosis of breast cancer using fluorescence and diffuse reflectance spectroscopy: A Monte-Carlo model-based approach. *Journal of Biomedical Optics*, 13(3), 034015.

How to cite this article: Carver GE, Locknar SA, Weaver DL, Stein JL, Stein GS. Real-time detection of breast cancer at the cellular level. *J Cell Physiol*. 2018;1–7.
<https://doi.org/10.1002/jcp.27451>